

# NATIONAL AIR INTELLIGENCE CENTER



SELECTED ARTICLES

19960715 095



Approved for public release:  
distribution unlimited

**HUMAN TRANSLATION**

NAIC-ID(RS)T-0138-96 5 June 1996

MICROFICHE NR:

SELECTED ARTICLES

English pages: 34

Source: Qiangjiguang Yu Lizishu (High Power Laser and Particle Beams), Vol. 2, Nr. 1, February 1990; pp. 85-100; 111-113

Country of origin: China

Translated by: Leo Kanner Associates  
F33657-88-D-2188

Requester: NAIC/TATD/Bruce Armstrong

Approved for public release: distribution unlimited.

THIS TRANSLATION IS A RENDITION OF THE ORIGINAL FOREIGN TEXT WITHOUT ANY ANALYTICAL OR EDITORIAL COMMENT STATEMENTS OR THEORIES ADVOCATED OR IMPLIED ARE THOSE OF THE SOURCE AND DO NOT NECESSARILY REFLECT THE POSITION OR OPINION OF THE NATIONAL AIR INTELLIGENCE CENTER.

PREPARED BY:

TRANSLATION SERVICES  
NATIONAL AIR INTELLIGENCE CENTER  
WPAFB, OHIO

## TABLE OF CONTENTS

Graphics Disclaimer .....	ii
Beam Control in Synthetic Aperture Systems, by Hu Zhiping, Zhou Hongyang, Le Shixiao .....	1
Wavefront Reconstruction from Wavefront Slope, by Wang Kaiyun .....	14
Preliminary Experiments of Laser Beam Transmission with Adaptive Optics Compensating Atmospheric Turbulence, by Jiang Wenhan, Yan Peiying, Dai Zichang, Li Bingcheng .....	30

#### GRAPHICS DISCLAIMER

All figures, graphics, tables, equations, etc. merged into this translation were extracted from the best quality copy available.

# Beam Control in Synthetic Aperture Systems

Hu Zhiping, Zhou Hongyang and Le Shixiao

(Southwest Computing Center, University of Electronic Science and Technology of China)

**Abstract:** In this paper, we discuss concepts of beam control in optical synthetic aperture systems in vacuo. The physical models for phase control of wavefront in transmitters are given. Computations were made for the models and the results are in agreement with the analysis. The results are also shown in three-dimensional figures. The effects of piston and tilt errors on the performance of the synthetic aperture systems are discussed and the computations are also given.

**Key Words:** synthetic aperture system, diffraction, beam control, beam combination, beam propagation, piston error, tilt error.

## 1. Introduction

To avoid nonlinear effects generated during intensive laser atmospheric propagation, it is necessary to reduce power density per laser unit area. A direct approach to doing this is to enlarge the optical system transmitting aperture scale, which, however, is restricted by a number of factors including optical material, optical quality, processing, manufacturing, etc. [1]. Moreover, a large-scale transmitting aperture system may not help realize rapid beam pointing and tracking [1]. The synthetic aperture system is an equivalently enlarged optically transmitting aperture system that has attracted attention in recent years as a method of avoiding nonlinear effects [2]. The synthetic aperture system is composed of a series of subaperture systems, which can independently transmit and transfer beams. It

can acquire an extremely high power density through phase control over individual subaperture systems transmitting a beam wavefront to realize noncoherent and coherent synthesis of individual beams at the target. Since every subaperture system is easy to control and manipulate, the synthetic aperture system appears helpful in realizing rapid beam pointing and tracking.

## 2. Phase Control Physical Models and Computer Simulation Demonstration

Generally, when propagating in vacuo, a beam can be described with Fresnel diffraction equation as follows:

$$\begin{aligned}
 U(x, y) &= \frac{e^{jkz} \exp\left[\frac{jk}{2z}(x^2 + y^2)\right]}{j\lambda z} \iint_{-\infty}^{\infty} U_0(x_1, y_1) \exp\left[\frac{jk}{2z}(x_1^2 + y_1^2)\right] \\
 &\quad \cdot \exp\left[-2\pi j\left(\frac{x}{\lambda z}x_1 + \frac{y}{\lambda z}y_1\right)\right] dx_1 dy_1 \\
 &= A(x, y, z) F\left\{U_0(x_1, y_1) \exp\left[\frac{jk}{2z}(x_1^2 + y_1^2)\right]\right\} \Big|_{\frac{x}{\lambda z}}^{\frac{y}{\lambda z}}
 \end{aligned} \tag{1}$$

where  $A(x, y, z) = e^{jkz} \cdot \exp[jk(x^2 + y^2)/2z]/j\lambda z$ ;  $F\{\cdot\}$  is the Fourier transform;  $k$  is number of waves;  $U_0(x_1, y_1)$  and  $U(x, y)$ , respectively, are the transmitting optical field distribution and the receiving optical field distribution. Eq. (1) serves as the foundation for computer simulation.

Beams generated by a laser device system are usually Gaussian beams, while beams transmitted by a laser device which operates on basement diaphragm can be expressed as:

$$U_0(r_1) = \frac{A}{b} \text{Gaus}\left(\frac{r_1}{b}\right) q\left(r_1, \frac{1}{\lambda R}\right) P_t(r_1) \tag{2}$$

where  $r_1^2 = x_1^2 + y_1^2$ ;  $\text{Gaus}(r_1/b) = \exp(-\pi r_1^2/b^2)$ ;  $q(r_1, 1/\lambda R) = \exp(j\pi r_1^2/\lambda R)$ ;  $b$  is the beam radius;  $R$  is beam wavefront curvature radius and  $A$  is a complex constant. For convenience in analysis, we will stipulate thereafter that:  $A \equiv 1$ ;  $P_t(r_1)$  is the transmission system optical-pupil function,  $d$  is the optical pupil diameter,

then

$$P_i(r_i) = \begin{cases} 1 & , \quad x_i^2 + y_i^2 < (d/2)^2 \\ 1/2 & , \quad x_i^2 + y_i^2 = (d/2)^2 \\ 0 & , \end{cases} \quad (3)$$

and so on

Beam phase control is intended to realize beam pointing, transfer, noncoherent and coherent synthesis changing the phase distribution of subaperture systems transmitting beam wavefront phase distribution.

#### 1) Beam Pointing

(1) Vertical Pointing. Vertical pointing signifies converging transmitted beams at a particular point on the transmitting optical pupil axial line. It can be proved [5] that if the transmitting optical field wavefront is multiplied by a phase factor

$$TP(x_i, y_i) = q^* \left( r_i, \frac{1}{\lambda f} \right), \quad \frac{1}{f} = \frac{1}{z} + \frac{1}{R}$$

and satisfies  $b/d=0.791$ , with "\*" as the complex conjugacy sign, then transmitting optical field will turn into

$$U_0(x_i, y_i) = U_0(x_i, y_i) \cdot TP(x_i, y_i) \quad (4)$$

Here the  $U_0(x_i, y_i)$  transmitted optical field converges at distance  $z$  on the axial line.  $TP(x_i, y_i)$  is referred to as vertical pointing factor.

(2) Horizontal pointing (transfer). Horizontal pointing refers

to horizontal translation of the beam convergent point. The Fourier transform is translational in nature [6]

$$F\{f(x_1, y_1) \exp[2j\pi(\xi_0 x_1 + \eta_0 y_1)]\} = F[f(x_1, y_1)] \Big|_{\substack{x=\xi_0 \\ y=\eta_0}}$$

If the transmitted wavefront is multiplied by a phase factor

$$TA(x_1, y_1, x_0, y_0) = \exp\left\{2j\pi\left[\frac{x_1 - x_0}{\lambda z} x_1 + \frac{y_1 - y_0}{\lambda z} y_1\right]\right\}$$

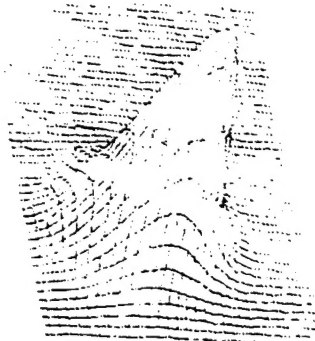
then the transmitting optical field will become

$$U_0(x_1, y_1) = U_0(x_1, y_1) TA(x_1, y_1, x_0, y_0) \quad (5)$$

Here the beam intensity at the point  $(x_0, y_0)$  has been translated to the point  $(x_1, y_1)$ . Therefore,  $TA(x_1, y_1, x_0, y_0)$  is called the horizontal pointing factor.



0.158241E-03



0.154951E-03

Fig. 1. Beam vertical pointing  $(x_1 = y_1 = 0)$  Fig. 2 Beam horizontal pointing  $(x_1 = y_1 = -10m)$

A simulation demonstration of typical parameters:  $\lambda=1\mu m$ ,  $z=1000km$ , and  $d=1m$  was conducted on a "Milky Way" computer with a rapid Fourier-transform algorithm (integrating point and sampling point were both selected as  $2^6=64$ ). Figs. 1 and 2 show computer-plotted three-dimensional configurations of optical field intensities transmitted by a single-aperture system. Fig. 2 displays horizontal translation of the pointing point in Fig. 1 ( $x_1=y_1=-10m$ ). The numbers in Fig. 2 suggest the peak intensity values (relative values). It can be seen that the peak intensity

values remain the same before and after horizontal pointing (the slight difference in the third decimal point is caused by algorithmic errors), which indicates that theoretical analysis conforms to calculations.

## 2) Beam Synthesis

Coherent and noncoherent beam power synthesis can be achieved at the target through phase control of individual subaperture systems transmitting the optical field wavefront. As shown in Fig. 3, the system consists of 16 subapertures, and the related parameters are also indicated in the figure.

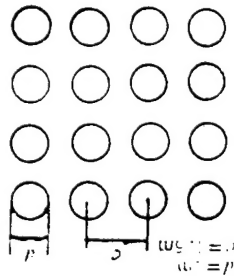
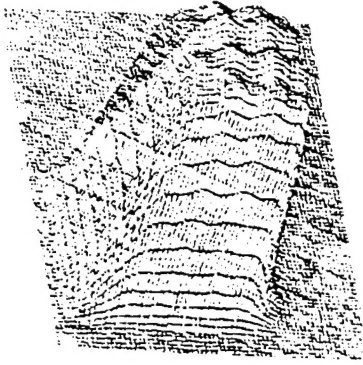


Fig. 3 Example of synthetic aperture system

(1) Noncoherent synthesis. All subaperture systems transmitting optical field intensity peaks are aimed and converged at the same point by using the foregoing beam pointing and transfer methods. Under this scenario, the peak intensity of the entire system is simply a stack of peak light intensities transmitted by individual subaperture systems. Fig. 4 indicates how the branch aperture system transmitted optical fields converge on their respective axial lines. Fig. 5 shows that individual subaperture systems transmitting optical fields have been aimed and converged on the same point, and beam power noncoherent synthesis was realized. Obviously, the peak intensity in Fig. 5 is 16 times that of individual subaperture systems as shown in Fig. 1.



0.244112E-03

Fig. 4. Noncoherent beam propagation



0.248361E-02

Fig. 5. Noncoherent beam synthesis

(2) Coherent synthesis. By changing the subaperture systems transmitting the optical field wavefront phases, all their optical fields are aimed and converged at the same point to achieve a coherent optical field stack instead of simple light intensity stack. To realize coherent beam synthesis, it should be ensured that individual beams have the same phase or phase difference equal to  $2\pi$ -integer fold at their common pointing point. Suppose subaperture central coordinates are  $x_s(i,j)$ ,  $y_s(i,j)$ ,  $(i,j=1,2,3,4)$ , subaperture systems transmitting the wavefronts  $U_{0ij}(x_1, y_1)$  are multiplied by the vertical and horizontal pointing factors and then by the phase control factor  $TC=[x, (i,j), y(i,j)]=\exp\{(\pi j/\gamma z)[x_s^2(i,j)+y_s^2(i,j)]\}$  [7] i.e.

$$U_{0ij}''(x_1, y_1) = U_{0ij}(x_1, y_1) \cdot TP[x_1, y_1, x_s(i,j), y_s(i,j)] \cdot TA[x_1, y_1, x_s(i,j), y_s(i,j), x_1, y_1] \cdot TC[x_s(i,j), y_s(i,j)] \quad (6)$$

then the individual beams will converge at the common pointing point  $(x_t, y_t, z)$ , and have the same phase or have a phase difference equal to  $2\pi$  integer fold, thus realizing coherent beam synthesis of individual beams. The proof is given as follows.

Here,

$$U_{0ij}(x_1, y_1) = \frac{1}{b_{ij}} \text{Gaus} \left( \frac{r_{1ij}}{b_{ij}} \right) q(r_{1ij}, \frac{1}{\lambda R_{ij}}) P_i(r_{1ij}),$$

$$r_{1ij}^2 = [x_1 - x_s(i, j)]^2 + [y_1 - y_s(i, j)]^2.$$

$$TP[x_1, y_1, x_s(i, j), y_s(i, j)] = q^* \left( r_{1ij}, \frac{1}{\lambda f_{ij}} \right), \quad \frac{1}{f_{ij}} = \frac{1}{z} + \frac{1}{R_{ij}}.$$

$$TA[x_1, y_1, x_s(i, j), y_s(i, j), x_i, y_i] = \exp \left\{ 2\pi j \left[ \frac{x_i - x_s(i, j)}{\lambda z} x_1 + \frac{y_i - y_s(i, j)}{\lambda z} y_1 \right] \right\}$$

The transmitted optical field of the entire system is

$$U_0(x_1, y_1) = \sum_{i=1}^4 \sum_{j=1}^4 U_{0ij}^*(x_1, y_1)$$

It is known from Eq. (1) that the receiving optical field is

$$U(x, y) = A(x, y, z) F \left\{ \sum_{i=1}^4 \sum_{j=1}^4 U_{0ij}^*(x_1, y_1) \exp \left[ \frac{jk}{2z} (x_1^2 + y_1^2) \right] \right\} \Big|_{\frac{1}{\lambda z}}$$

Substituting Eq. (6) for the foregoing equation, we obtain

$$\begin{aligned} U(x, y) &= A(x, y, z) F \left\{ \sum_{i=1}^4 \sum_{j=1}^4 \frac{1}{b_{ij}} \text{Gaus} \left( \frac{r_{1ij}}{b_{ij}} \right) q \left( r_{1ij}, \frac{1}{\lambda R_{ij}} \right) P_i(r_{1ij}) \right. \\ &\quad \cdot q^* \left( r_{1ij}, \frac{1}{\lambda f_{ij}} \right) \exp \left[ 2\pi j \left( \frac{x_i - x_s(i, j)}{\lambda z} x_1 + \frac{y_i - y_s(i, j)}{\lambda z} y_1 \right) \right] \\ &\quad \cdot \exp \left[ \frac{\pi j}{\lambda z} (x_s^2(i, j) + y_s^2(i, j)) \right] \exp \left[ \frac{jk}{2z} (x_1^2 + y_1^2) \right] \Big\} \Big|_{\frac{1}{\lambda z}} \\ &= A(x, y, z) F \left\{ \sum_{i=1}^4 \sum_{j=1}^4 \text{Gaus} \left( \frac{r_{1ij}}{b_{ij}} \right) P_i(r_{1ij}) \exp \left( j\pi \frac{r_{1ij}^2}{\lambda R_{ij}} \right) \exp \left( -j\pi \frac{r_{1ij}^2}{\lambda f_{ij}} \right) \right. \\ &\quad \cdot \exp \left\{ \frac{\pi j}{\lambda z} [(x_1 - x_s(i, j))^2 + (y_1 - y_s(i, j))^2] \right\} \exp \left[ 2\pi j \left( \frac{x_i}{\lambda z} x_1 + \frac{y_i}{\lambda z} y_1 \right) \right] \Big\} \Big|_{\frac{1}{\lambda z}} \\ &= A(x, y, z) F \left\{ \sum_{i=1}^4 \sum_{j=1}^4 \frac{1}{b_{ij}} \text{Gaus} \left( \frac{r_{1ij}}{b_{ij}} \right) P_i(r_{1ij}) \exp \left[ 2\pi j \left( \frac{x_i}{\lambda z} x_1 + \frac{y_i}{\lambda z} y_1 \right) \right] \right\} \Big|_{\frac{1}{\lambda z}} \end{aligned}$$

where

$$\frac{1}{f_{ij}} = \frac{1}{R_{ij}} + \frac{1}{z}.$$

When  $b_{ij} = b$ ,

$$\begin{aligned} U(x, y) &= A(x, y, z) F \left\{ \sum_{i=1}^4 \sum_{j=1}^4 \frac{1}{b} \text{Gaus} \left( \frac{r_{1ij}}{b} \right) P_i(r_{1ij}) \right\} \Big|_{\frac{1}{\lambda z}} \\ &= A(x, y, z) \times 16 \times F \left\{ \frac{1}{b} \text{Gaus} \left( \frac{r_1}{b} \right) P_i(r_1) \right\} \Big|_{\frac{1}{\lambda z}} \\ &\leq 16 \cdot A(x, y, z) F \left\{ \frac{1}{b} \text{Gaus} \left( \frac{r_1}{b} \right) P_i(r_1) \right\} \Big|_0^0, \quad (x = x_1, y = y_1) \end{aligned}$$

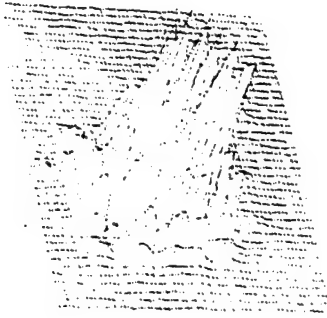
Thus, the peak light intensity of the receiving optical field is

$$I(x_t, y_t) = |U(x_t, y_t)|^2 = 16^2 \times |A(x, y, z)|^2 F \left\{ \frac{1}{b} \text{Gaus} \left( \frac{r_t}{b} \right) P_t(r_t) \right\}_0^2 \quad (7)$$

It is known, therefore, that beams achieve coherent synthesis at the point  $(x_t, y_t, z)$ , and the peak light intensity is  $16^2$  times that of the optical field transmitted by the single subaperture system at that point.

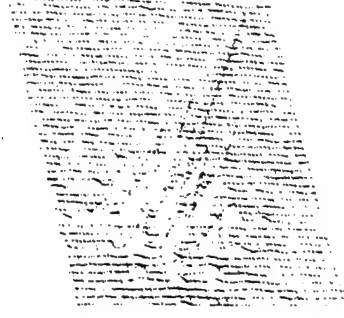
Figure 6 shows the receiving optical field intensity distribution before the optical field wavefront transmitted by the subaperture system has been multiplied by the phase control factor  $TC[x_t(i, j), y_t(i, j)]$ . Owing to destructive interference, however, coherent beam synthesis has not been realized at the common pointing point, while the intensity peak values have been shifted to surrounding side bands. On the contrary, Fig. 7 shows the receiving optical field intensity distribution after the optical field wavefront transmitted by the subaperture system has been multiplied by phase control factor

$TC[x_t(i, j), y_t(i, j)]$ . Owing to supplementary interference, individual beams have achieved coherent beam synthesis at the common pointing point  $(x_t, y_t, z)$ . At the same time, intensities on the side bands have greatly reduced, while the peak intensity at the common pointing point  $(x_t, y_t, z)$  has greatly increased. The numbers in the figure suggest that the peak intensity is approximately 256 times that of single aperture system (not exactly 256 times because of algorithmic errors).



0.401820 E-02

Fig. 6. Beam synthesis  
( $x_t=y_t=0$ )



0.405527 E-02

Fig. 7. Coherent beam  
synthesis ( $x_t=y_t=0$ )

### 3. Effect of Subaperture Piston and Tilt Errors

The foregoing description is the ideal situation, without considering the effect of subaperture system phase modulation errors on synthesized peak intensity at the target spot. Therefore, we need to discuss the effect of piston and tilt errors caused by phase modulation.

Suppose the synthetic aperture system has a total area  $S$ , composed of  $N$  subapertures, and each subaperture system has an area  $S/N=\pi D^2/4$ , with  $D$  as its diameter. For convenience in analysis, the far-field conditions (Fraunhofer's diffraction) have been taken into account. Let us assume that the beams transmitted by the subaperture systems converge at distance  $z$ , then the far-field optical field distribution is

$$\begin{aligned}
 U(x, y) &= \frac{e^{jkz} \cdot \exp\left[\frac{jk}{2z}(x^2+y^2)\right]}{j\lambda z} \iint U_0(x_1, y_1) \\
 &\quad \cdot \exp\left\{-2\pi j\left(\frac{x}{\lambda z}x_1 + \frac{y}{\lambda z}y_1\right)\right\} dx_1 dy_1 \\
 &= \frac{e^{jkz} \cdot \exp\left[\frac{jk}{2z}(x^2+y^2)\right]}{j\lambda z} \sum_{n=1}^N \iint U_n(x_1, y_1) \\
 &\quad \cdot \exp\left\{-2\pi j\left(\frac{x}{\lambda z}x_1 + \frac{y}{\lambda z}y_1\right)\right\} dx_1 dy_1
 \end{aligned}$$

Suppose  $U_{0n}(x_1, y_1) = (P/S)^{1/2} \exp\{jk[a_n + b_n(x_1 - x_{sn}) + c_n(y_1 - y_{sn})]\}$ , where  $P$  is the total transmission power,  $(x_{sn}, y_{sn})$  is the subaperture central coordinate, the  $U_{0n}(x_1, y_1)$  phase term is the residual-error term, caused by subaperture system phase modulation,  $a_n$  is the piston error,  $b_n$ ,  $c_n$  are tilt errors. Again let us suppose  $a_n$ ,  $b_n$  and  $c_n$  are independent Gaussian random variables that can satisfy the condition  $\langle a_n \rangle = \langle b_n \rangle = 0$ ,

$\langle a_n^2 \rangle = \sigma_a^2$ ,  $\langle b_n^2 \rangle = \langle c_n^2 \rangle = \sigma_t^2$ , where  $\langle \rangle$  is the ensemble average.

The average light intensity distribution at the focal plane is

$$\begin{aligned} \langle I(x, y) \rangle &= (P/S\lambda^2 z^2) \left\{ \sum_n \iint_{s_n} dx_1 dy_1 \iint_{s_n} dx_2 dy_2 \exp\left[-2\pi j\left(\frac{x}{\lambda z} x_1 + \frac{y}{\lambda z} y_1\right)\right] \right. \\ &\quad \cdot \langle \exp[jk b_n(x_1 - x_2)] \rangle \langle \exp[jk c_n(y_1 - y_2)] \rangle \\ &\quad + \sum_{n \neq m} \iint_{s_n} dx_1 dy_1 \iint_{s_m} dx_2 dy_2 \exp\left[-2\pi j\left(\frac{x}{\lambda z} x_1 + \frac{y}{\lambda z} y_1\right)\right] \\ &\quad \cdot \langle \exp(jk a_n) \rangle \langle \exp(-jk a_m) \rangle \langle \exp[jk b_n(x_1 - x_{sn})] \rangle \\ &\quad \cdot \langle \exp[-jk b_m(x_2 - x_{sm})] \rangle \langle \exp[jk c_n(y_1 - y_{sn})] \rangle \\ &\quad \cdot \langle \exp[-jk c_m(y_2 - y_{sm})] \rangle \left. \right\} \\ &= (P/S\lambda^2 z^2) \left\{ \sum_n \iint_{s_n} dx_1 dy_1 \iint_{s_n} dx_2 dy_2 \exp\left[-2\pi j\left(\frac{x}{\lambda z} x_1 + \frac{y}{\lambda z} y_1\right)\right] \right. \\ &\quad \cdot \exp\left\{-k^2 \sigma_t^2 [(x_1 - x_2)^2 + (y_1 - y_2)^2]/2\right\} + \sum_{n \neq m} \iint_{s_n} dx_1 dy_1 \\ &\quad \cdot \iint_{s_m} dx_2 dy_2 \exp\left[-2\pi j\left(\frac{x}{\lambda z} x_1 + \frac{y}{\lambda z} y_1\right)\right] \cdot \exp(-k^2 \sigma_a^2) \\ &\quad \cdot \exp\left\{-k^2 \sigma_t^2 [(x_1 - x_{sn})^2 + (y_1 - y_{sn})^2 + (x_2 - x_{sm})^2 + (y_2 - y_{sm})^2]/2\right\} \left. \right\} \end{aligned}$$

by coordinate conversion, we obtain

$$\begin{aligned} \langle I(x, y) \rangle = (P/S\lambda^2 z^2) \left\{ 4SD^2 \int_0^1 \rho d\rho \exp(-k^2 \sigma_T^2 D^2 \rho^2 / 2) \cdot [\cos^{-1}(\rho) \right. \\ \left. - \rho \sqrt{1-\rho^2}] J_0(kDr\rho/z) + 4\pi^2 \exp(-k^2 \sigma_0^2) \right. \\ \cdot \sum_{n \neq m} \exp[-2\pi j(\frac{x_r - x_m}{\lambda z} x + \frac{y_r - y_m}{\lambda z} y)] \\ \cdot \left. \left[ \int_0^{D/z} r_1 dr_1 \exp(-k^2 \sigma_T^2 r_1^2 / 2) \times J_0(krr_1/z) \right]^2 \right\} \end{aligned}$$

where  $r^2 = x^2 + y^2$ ,  $J_0$  is the zero-valent Bessel function. Obviously

$$\begin{aligned} \langle I(0) \rangle = (P/S\lambda^2 z^2) \left\{ 4SD^2 \int_0^1 \rho d\rho \exp(-k^2 \sigma_T^2 \rho^2 / 2) [\cos^{-1}(\rho) \right. \\ \left. - \rho \sqrt{1-\rho^2}] + 4\pi^2 \exp(-k^2 \sigma_0^2) (N^2 - N) \left[ \int_0^{D/z} r_1 \exp(-k^2 \sigma_T^2 r_1^2 / 2) dr_1 \right]^2 \right\} \end{aligned}$$

finally

$$\begin{aligned} \langle I(0) \rangle = (P/S\lambda^2 z^2) \left\{ [8/(Nk^2 \sigma_T^2 D^2)] [1 - \exp(-k^2 \sigma_T^2 D^2 / 4)] \right. \\ \cdot [I_0(k^2 \sigma_T^2 D^2 / 4) + I_1(k^2 \sigma_T^2 D^2 / 4)] + [64/(N^2 k^4 \sigma_0^4 D^4)] \\ \cdot (N^2 - N) \exp(-k^2 \sigma_0^2) [1 - \exp(-k^2 \sigma_T^2 D^2 / 8)]^2 \left. \right\} \end{aligned}$$

where  $I_0$  and  $I_1$  are, respectively, the zero-valent and monovalent updated Bessel functions [8].

Let  $P_0 = \sigma_0 / \lambda$ ,  $P_T = \sigma_T D / \lambda$ , and divide  $\langle I(0) \rangle$  by its diffraction limit value:  $P / S \lambda^2 z^2$ , we obtain the Strior ratio

$$I_{rel} = (2/N\pi^2 P_T^2) \{ 1 - \exp(-\pi^2 P_T^2) \cdot [I_0(\pi^2 P_T^2) + I_1(\pi^2 P_T^2)] \} + 4[(N-1)/(N\pi^2 P_T^2)] \exp(-4\pi^2 P_0^2) \cdot [1 - \exp(-\pi^2 P_T^2/2)]^2 \quad (8)$$

Obviously,  $I_{rel}$  represents the effect of the subaperture system phase modulation error ( $P_0$ ,  $P_T$ ) on the synthesized peak intensity on the focal plane, generally  $I_{rel} \leq 1$ . Fig. 8 shows the variation curve of  $I_{rel}$  with  $P_T$  to different  $P_0$  values in the case of  $N=16$ , which was obtained with numerical computations on Eq. (8).

Fig. 8 indicates that the larger the  $P_0$  and  $P_T$  (the larger the phase modulation piston and tilt errors), the greater the decrease that the synthesized peak intensity can be subjected to.

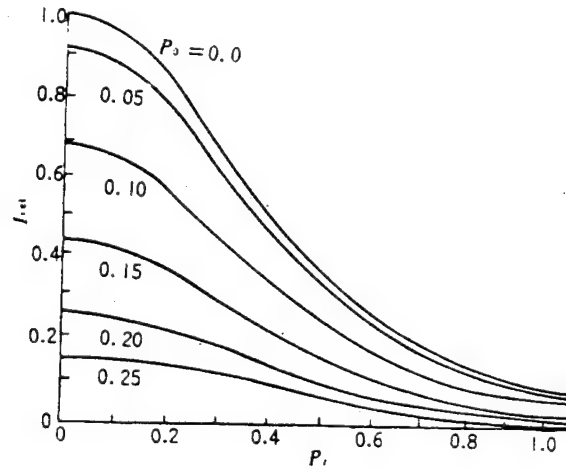


Fig. 8 Variation of  $I_{rel}$  with  $P_T$

#### 4. Conclusions

In this paper, we discussed the concept of optically synthetic aperture system beam wavefront phase control in vacuo, and we carried out a corresponding numerical simulation on a "Milky Way" computer with rapid Fourier transform. Finally, we also made an initial analysis and calculation of the effect of subaperture system phase modulation errors. These studies, however, may be quite tentative, without taking actual atmospheric effects into consideration. Therefore, further studies are scheduled to be undertaken on beam wavefront phase control under the effect of various linear and nonlinear factors in the atmosphere.

Acknowledgements. Our thanks go to research fellow Li Youping and associate research fellow Sun Jingwen from the China Academy of Engineering Physics for their counsel and assistance.

This paper was received for publication on January 2, 1989.  
The revised paper was received on April 3, 1989.

#### References

- [1] American Physical Society Study Group. Science and Technology of Directed Energy Weapons. *Rev. Mod. Phys.*, 59(3), 87, Part II, (1987).
- [2] J. S. Fender. Synthetic Aperture Systems. *Proc. SPIE*, 440, (1983).
- [3] 黄婉云编. 傅里叶光学教程. 北京师范大学出版社, 98 (1985).
- [4] J. D. 加斯基尔. 线性系统·傅里叶变换·光学. 人民教育出版社, 420 (1981).
- [5] 同上, p. 390, 438.

# Wavefront Reconstruction from Wavefront Slope

Wang Kaiyun

(Chinese Academy Of Engineering Physics)

**Abstract:** Based on the model of Southwell et al., we introduce two kinds of zonal wavefront reconstruction models in which subapertures are arranged in a geometry of equilateral triangle. The least-squares solution, the minimum norm solution, and the matrix iterative solution are given. The model analysis is carried out on the circular aperture, which is often used by many researchers. Error propagation properties for the two models are evaluated and compared with Southwell's model.

**Key Words** wavefront reconstruction, zonal method, model method, successive over-relaxation method

## 1. Introduction

Adaptive optics systems have widespread application prospects in improving beam quality and imaging quality. In principle, this system serves to make advance compensation for wavefront errors, which includes wavefront detection, wavefront reconstruction processing and wavefront deformable mirror simulation.

This paper is devoted to an evaluation of wavefront phases with a set of discrete phase slope information, i.e. wavefront reconstruction. In such case, evaluation is made either of phase values in local zones or of aperture function coefficients, depending on the needs. Similarly, there are two evaluation methods: zonal method and model method.

Southwell [1] proposed three major factors in comparing

various reconstruction models, namely: (1) compatibility: whether or not a particular model fits the slope measurement mode given by a detector; (2) numerical complexity: whether or not there is a problem with convergence, computer storage capacity, and computation velocity and (3) error propagation: what effect slope measurement noise may have on phase evaluation.

Based on these three principles, this paper gives an analysis and computations for reconstruction models.

The retarders of deformable mirrors that are used to correct wavefront distortion can be arranged in different ways. As far as the wavefront reconstruction model method is concerned, detector subapertures can be arranged in the same way as, or in a different way from the retarders, while the zonal method requires both in the same arrangement. This paper limits its attention to two subaperture arrangements involved in the zonal method: the square arrangement and the equilateral triangle arrangement.

For the square subaperture arrangement, Southwell [1], Hudkin [2] and Fried [3] advanced their respective reconstruction models. On this basis, two additional reconstruction models are introduced in this paper involving the equilateral triangle arrangement. Just as in the Fried [2] and Southwell [1] models, here the x- and y- direction slope measurement rates are coincident (to suit the Hartmann sensor). One of the new models introduced is even superior to Southwell's in terms of error propagation properties, partly because sampling of the equilateral triangle subaperture arrangement is even more uniform than that with the square arrangement.

## 2. Wavefront Reconstruction Models

Fig. 1 shows two detector subaperture arrangements in a circular aperture with each subaperture capable of measuring the

x- and y-direction slopes in that particular zone at the same time. Both arrangements are applicable to the Hartmann sensor.

When the center of a given subaperture lies inside the aperture, the aperture is considered to enclose that subaperture. Of course, such consideration may not conform to reality. If subapertures are all required to be arranged inside an aperture, such requirement can be easily achieved by appropriately reducing their diameters.

Three wavefront reconstruction equations can then be derived for the two arrangements as shown in Fig. 1.

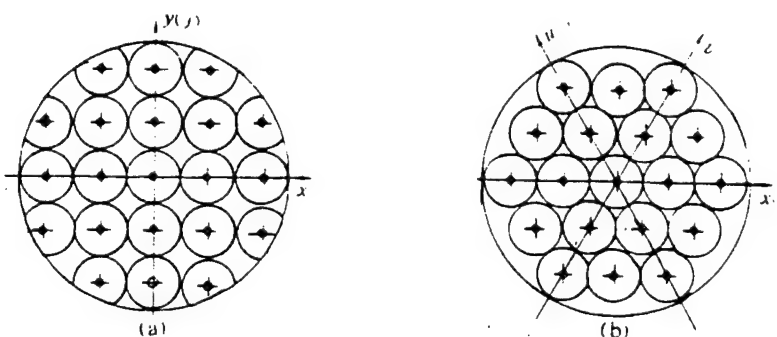


Fig. 1. Detector subaperture arrangements. Horizontal lines mark the x-direction slope, while plumb lines mark the y-direction slope; circular points are the phase points to be evaluated. (a) square arrangement proposed by Southwell [1]; (b) equilateral triangle arrangement with points located by x- and u-direction ordinal numbers.

#### 1) Southwell Equation--Model I

As seen in Fig. 2, slope measurement data and phases to be evaluated are all located on subaperture centers. Owing to the small value of  $h$ , the following linear relations can be taken as established in any subzone

$$\frac{1}{2} (S_{i-1,j}^x + S_{i,j}^x) = \frac{1}{h} (\Phi_{i+1,j} - \Phi_{i,j}) \quad \frac{1}{2} (S_{i,j+1}^y + S_{i,j}^y) = \frac{1}{h} (\Phi_{i,j+1} - \Phi_{i,j}) \quad (1)$$

where  $\Phi$  is phase,  $S$  is slope.

According to this model, slopes inside zones keep changing and therefore, the phases to be evaluated will change by parabolically.

## 2) Model II

In Fig. 1(B), equations similar to Eq. (1) can be easily derived in the  $x$ - and  $u$ -directions from model I. Referring to Fig. 3, we obtain

$$\frac{1}{2} (S_{i-1,j}^x + S_{i,j}^x) = \frac{1}{h} (\Phi_{i+1,j} - \Phi_{i,j}) \quad \frac{1}{2} (S_{i,j+1}^y + S_{i,j}^y) = \frac{1}{h} (\Phi_{i,j+1} - \Phi_{i,j}) \quad (2)$$

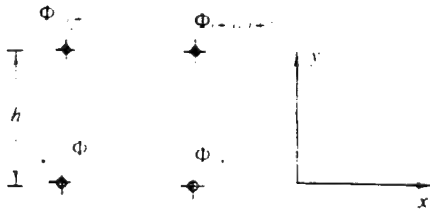


Fig. 2.

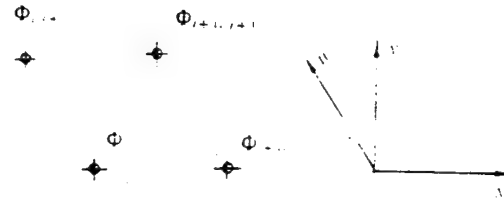


Fig. 3.

Here, we have changed only the subaperture arrangement, while the  $x$ - and  $y$ -direction slopes are still the measurement targets of subapertures. The slope in the  $u$ -direction can be solved through the following relations:

$$S^u = -\frac{1}{2} S^x - \frac{\sqrt{3}}{2} S^y \quad (3)$$

## 3) Model III

In the equilateral triangle arrangement of subapertures, their distribution is symmetric to the  $x$ -,  $u$ - and  $y$ -axes as shown in (B) of Fig. 1. Considering all these axes, the following relation can be derived from Fig. 4:

$$\frac{1}{2} (S_{i+1,j}^x + S_{i,j}^x) = \frac{1}{h} (\Phi_{i+1,j} - \Phi_{i,j}) \quad (4)$$

$$\frac{1}{2} (S_{i,j+1}^y + S_{i,j}^y) = \frac{1}{h} (\Phi_{i,j+1} - \Phi_{i,j})$$

$$\frac{1}{2} (S_{i+1,j+1}^x + S_{i,j}^x) = \frac{1}{h} (\Phi_{i+1,j+1} - \Phi_{i,j})$$

where the slope in the  $v$  direction is

$$S^v = \frac{1}{2} S^x + \frac{\sqrt{3}}{2} S^y \quad (5)$$

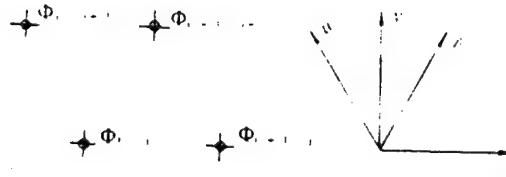


Fig. 4

### 3. Minimum Mathematical Power Solution

All coupled equations similar to (1), (2) and (4) can be listed respectively in the entire aperture, which can be expressed with the following matrix:

$$DS = A\Phi \quad (6)$$

where  $S$  is a vector that includes all slope information (in the  $x$ - and  $y$ -directions), while  $\Phi$  is the vector which includes all phases to be evaluated. Suppose the number of subapertures located on aperture diameter is  $N$ , then the number of  $A$  elements is directly proportional to  $N^4$ , the number of  $D$  elements is two times that of  $A$ , and both  $A$  and  $D$  are extremely sparse matrixes.

By multiplying both sides of (6) by  $\mathbf{A}^+$  (transposed matrix of  $\mathbf{A}$ ) on the left, we obtain

$$(\mathbf{A}^+ \mathbf{A}) \Phi = \mathbf{A}^+ \mathbf{D} \mathbf{S} \quad (7)$$

This is a linear coupled equation. Generally, by multiplying both its sides by the  $(\mathbf{A}^+ \mathbf{A})$  reverse matrix on the left, the standard minimum mathematical power solution can be obtained. In fact, however, standard minimum mathematical power solution can not be obtained since  $(\mathbf{A}^+ \mathbf{A})$  is an ill-conditioned matrix, i.e. its order is not complete, which does not mean that we cannot acquire a meaningful wavefront from Eq. (7), but it means that we cannot use the standard complementary technique.

#### 1) Standard Minimum Mathematical Power Solution

Since  $(\mathbf{A}^+ \mathbf{A})$  is an ill-conditioned matrix, we need to transform the matrix  $\mathbf{A}$  structure. The method used is to take a phase on a certain point of the wavefront as zero, and thereby, one column has been removed from matrix  $\mathbf{A}$ . Then, the remaining matrix  $\mathbf{A}_r$  has a complete order and admits the use of the of standard minimum mathematical power solution:

$$\Phi = [\mathbf{A}_r^+ \mathbf{A}_r]^{-1} \mathbf{A}_r^+ \mathbf{D} \mathbf{S} \quad (8)$$

#### 2) Minimum Mathematical Power Minimum Norm Solution

Although  $(\mathbf{A}^+ \mathbf{A})$  is an ill-conditioned matrix, augmented matrix  $\mathbf{A}_e$  can replace  $\mathbf{A}$  so as to make its order complete, by which the minimum mathematical power minimum norm solution can be obtained.

By removing the average phase from the wavefront phases to make the phase mean value equal to zero, the augmented matrix can

be introduced

$$A_s = \begin{bmatrix} A \\ A_s \end{bmatrix} \quad D_s = \begin{bmatrix} D \\ D_s \end{bmatrix}$$

where  $A_s$  is a line or matrix with element value equal to 1,  $D_s$  is a line or matrix with element value equal to 0. Subsequently,  $(A^+ A_s)$  is no longer ill-conditioned, therefore

$$\Phi = [A_s^+ A_s]^{-1} A_s^+ D_s, S = [A_s^+ A_s]^{-1} A_s^+ D S \quad (9)$$

If the wavefront reconstruction computations are made with (8) and (9), computer storage capacity is required to be at least  $2 \times N^4$ , where  $N$  is the number of subapertures on the aperture diameter. And when  $N$  exceeds a certain limit, it will be difficult for the computer to meet the internal storage requirement set by the matrix solution. Under this scenario, the matrix iterative method can be used to solve Eqs. (8) and (9).

#### 4. Matrix Iterative Solution

Iterative equations are generally solved by listing the nonzero matrix elements in Eq. (7). For convenience in editing programs, let us try a different method to solve the iterative equations.

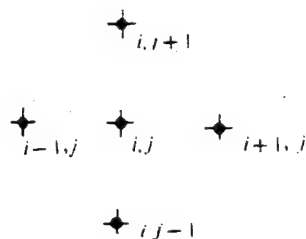


Fig. 5. Principal map in setting up the iterative equations of model I

In the first place, the iterative equations of model I are

setup. By studying Fig. 5, we obtain the following four equations:

$$\left. \begin{aligned} \Phi_{i-1,j} - \Phi_{i,j} &= \frac{h}{2} (S_{i-1,j}^x + S_{i,j}^x) & (a) \\ \Phi_{i,j} - \Phi_{i+1,j} &= \frac{h}{2} (S_{i,j}^x + S_{i+1,j}^x) & (b) \\ \Phi_{i,j+1} - \Phi_{i,j} &= \frac{h}{2} (S_{i,j+1}^y + S_{i,j}^y) & (c) \\ \Phi_{i,j} - \Phi_{i,j-1} &= \frac{h}{2} (S_{i,j}^y + S_{i,j-1}^y) & (d) \end{aligned} \right\} \quad (10)$$

In the foregoing equations, let

$$G_{i+1,j}^x = S_{i+1,j}^x + S_{i,j}^x, \quad G_{i-1,j}^x = S_{i,j}^x + S_{i-1,j}^x, \quad G_{i,j+1}^y = S_{i,j+1}^y + S_{i,j}^y, \quad G_{i,j-1}^y = S_{i,j}^y + S_{i,j-1}^y$$

$$- (a) + (b) - (c) + (d),$$

we obtain

$$\alpha_{i,j} \Phi_{i,j} - (\Phi_{i-1,j} + \Phi_{i+1,j} + \Phi_{i,j+1} + \Phi_{i,j-1}) = \frac{h}{2} (G_{i,j-1}^y - G_{i,j+1}^y + G_{i-1,j}^x - G_{i+1,j}^x) \quad (11)$$

where weighted coefficient

$$\alpha_{i,j} = \Phi_{i,j}: \text{ number of neighboring phase points } (2, 3, 4) \quad (12)$$

If the four neighboring phase points around  $\Phi_{i,j}$  are all present, **S** can be used to replace **G**. When a particular neighboring point phase of  $\Phi_{i,j}$  is actually missing,  $\Phi$  and **S** at that point can be taken as zero.

In Eq. (11), let

$$\begin{aligned} \bar{\Phi}_{i,j} &= \frac{1}{\alpha_{i,j}} (\Phi_{i-1,j} - \Phi_{i+1,j} + \Phi_{i,j+1} + \Phi_{i,j-1}) \\ \bar{\beta}_{i,j} &= \frac{h}{2} (G_{i,j-1}^y - G_{i,j+1}^y + G_{i-1,j}^x - G_{i+1,j}^x) \end{aligned}$$

Equation (11) can be simplified as

$$\Phi_{i,j} = \bar{\Phi}_{i,j} - \beta_{i,j} / \alpha_{i,j} \quad (13)$$

the above equation is the basis for the iterative algorithm. To speed up computations, the successive over-relaxation method (hereinafter SOR) with faster convergence was used in this paper, whose iterative equation can be expressed as

$$\Phi_{i,j}^{(m+1)} = \Phi_{i,j}^{(m)} + [\bar{\Phi}_{i,j}^{(m)} - \beta_{i,j} / \alpha_{i,j} - \Phi_{i,j}^{(m)}] \omega \quad (14)$$

where  $m$  is the iteration times,  $\bar{\Phi}_{i,j}^{(m)}$  is phase value at  $(i,j)$  obtained through  $m$  iterations,  $\bar{\Phi}_{i,j}^{(m)}$  is the mean value needed for the  $m+1$ -th iteration. Attenuation factor  $\omega$  is

$$\omega = \frac{2}{1 + \sin[\pi/(N+1)]} \quad (15)$$

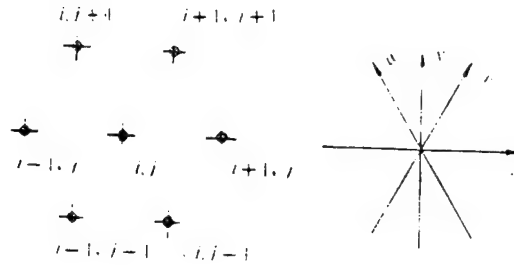


Fig. 6 Principle map of setting up iterative equations of model III

Since model II very much resembles model I, the model II iterative equation conforming to Eq. (14) in form can be acquired by replacing the  $y$ -axis by the  $u$ -axis in model I, during which the attenuation factor is

$$\omega = \frac{2}{1 + \sin[\pi/(3.7N)]} \quad (16)$$

where coefficients 3 and 7 in front of  $N$  are empirical values obtained through a large number of computations.

The iterative solution of model III should take into consideration not only the x- and u-axes, but also v-axis as seen in Fig. 6. If Eq. (14) is used to express the model III iterative solution, then the implications of individual terms are

$$\bar{\Phi}_{i,j} = (\Phi_{i-1,j} + \Phi_{i+1,j} + \Phi_{i,j-1} + \Phi_{i,j+1} + \Phi_{i-1,j+1} + \Phi_{i+1,j-1}) / z_{i,j} \quad (17)$$

$$z_{i,j} = \Phi_{i,j} \text{ number of neighboring phase points } (2,3,4,5,6) \quad (18)$$

$$\beta_{i,j} = \frac{h}{2} (G_{i-1,j}^x - G_{i+1,j}^x + G_{i,j-1}^y - G_{i,j+1}^y + G_{i-1,j+1}^x - G_{i+1,j-1}^x) \quad (19)$$

The empirical equation of  $\omega$  is

$$\omega = \frac{2}{1 + \sin\{\pi/[1.325(N-1)]\}} \quad (20)$$

## 5. Error Analysis

There are two error sources in carrying out wavefront reconstruction: one is algorithmic precision, and the other is measurement errors.

Algorithm precision signifies whether or not the minimum mathematical power process can precisely reconstruct the wavefront phases of random shapes, which virtually relies on the number of sample points on the wavefront shapes. Given the same number of radial subapertures, total subaperture number in models II and III is larger than that in model I in most cases, which will be favorable for increasing slope data sampling density and further, for increasing algorithmic precision.

On the other hand, wavefront errors caused by measurement errors depend on error propagation, which is expressed by noise coefficient  $C$ .  $C$  can be solved from the reconstruction equations.

Let the slope and phase errors be respectively,  $\sigma$  and  $\varepsilon$ , i.e.

$$S = S_0 \pm \sigma \quad (21)$$

$$\Phi = \Phi_0 \pm \varepsilon \quad (22)$$

According to Southwell's equation, we obtain

$$C = \frac{\langle \varepsilon^2 \rangle}{\langle \sigma^2 \rangle} = \frac{1}{(2R)^2} \sum_i \sum_k B_{ik}^2 \quad (23)$$

where  $\langle \varepsilon^2 \rangle$  is the mean square phase error,  $\langle \sigma^2 \rangle$  is the mean square slope error,  $R$  is aperture radius, matrix  $B$  is

$$B = (A_r^T A_r)^{-1} A_r^T D \quad (24)$$

An analysis will be given below of the error propagation performance of individual models in terms of Eq. (23).

First, compare the noise coefficients of the circular and square apertures. Since the total number of subapertures and number of radial subapertures  $N$  in a circular aperture do not affect mathematical relations, the total number of subapertures was taken as abscissa. Fig. 7 shows the computations over model I with the minimum mathematical power minimum norm method, in which the circular aperture displays a rather low noise coefficient and it obviously appears more advantageous for wavefront reconstruction than the square aperture under the same number of subapertures.

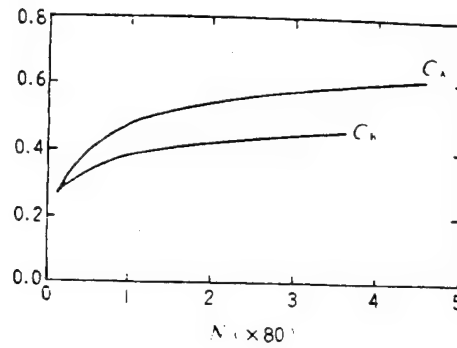


Fig. 7 Noise coefficient of model I  
 $C_A$  is square aperture while  $C_B$  is  
circular aperture; abscissa is total  
subaperture number; ordinate is noise  
coefficient (just as in Figs. 8 and 9)

Secondly, the compare error propagation performance of the foregoing three reconstruction models on the circular aperture as shown in Fig. 8. In this case, related data were also obtained with the minimum mathematical power minimum norm method, but due to the limitation of computer storage capacity (internal storage), the total subaperture number could not extend to zones above 421. Because of algorithmic defects, noise coefficient of model II turned out to be higher than that in the other two models. Model III exhibited a more uniform data sampling layout than model I, and the x-, y- and u-axes considered in its algorithm showed perfect symmetry, which led to the lowest noise coefficient and the best error propagation properties.

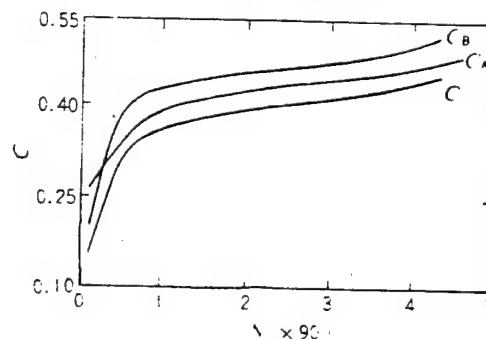


Fig. 8 Noise Coefficient Comparison between  
Individual Reconstruction Models.  $C_A$ ,  $C_B$  and  
 $C$  respectively represent models I, II and III

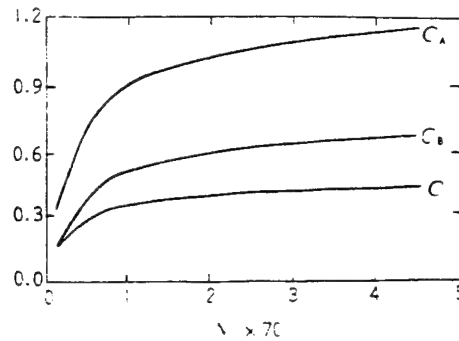


Fig. 9 Effect of Different Solutions on Noise Coefficient (Model III).  $C_A$  and  $C_B$  are two standard minimum mathematical power solutions while  $C$  is minimum mathematical power minimum norm solution

Lastly, let us investigate the two minimum mathematical power solutions. Fig. 9 shows that  $C_A$  and  $C_B$  are the noise coefficients of the two minimum mathematical power solutions, the zero phase of  $C_A$  is located on the subaperture distribution angle while that of  $C_B$  is selected at the aperture center, and  $C$  is the noise coefficient of the minimum mathematical power minimum norm solution, which is, in fact, a minimum mathematical power solution with phase mean value equal to zero. The minimum mathematical power minimum norm solution shows the lowest noise coefficient, and the difference between  $C_A$  and  $C_B$  is more than two times than between  $C_B$  and  $C$ . During computations by using the iterative method, a certain phase has to be subtracted from all computed values with each iteration. This phase value is, in the case of  $C_A$ ,  $C_B$  and  $C$ , respectively, a mean value of the phase on the subaperture distribution angle, the phase in the aperture center, and all phases on the aperture that appears more complex in computations. Therefore, to meet both computation precision and computation speed, it is desirable to use the iterative method with zero phase selected at the aperture center.

## 6. Comparison between Matrix Solution and Iterative Solution

Them matrix solution differs from the iterative solution (SOR method) not only as to algorithm, but as to the computation load and storage space needed as well. Eqs. (9) and (14) indicate that the two indices in the former are both directly proportion to  $N^4$ , while the storage space required in the latter is directly proportional to  $N^2$ , and its computation load is associated with not only  $N$ , but also with the number of iterations. Table 1 shows that the number of iterations is approximately directly proportional to  $N$ , and total computational load for one iteration is directly proportional to  $N^2$ , and consequently, the total computational load for the iterative method should be directly proportional to  $N^3$ . Table 1 also shows that when  $N$  is small, the computation time required by the iterative solution is longer than the serial computation time needed for the matrix solution, but when  $N$  surpasses 9, the relation becomes the opposite. However, in the case of parallel computations, the matrix solution can increase the computational speed by two orders (which is determined by computer parallelism), for which the SOR iteration method is by no means a match.

Table 1 Comparison between Iteration Solution and Matrix Solution in Terms of Computational Load

The reconstruction model is Southwell's [1], with its wavefront mode as  $W=2.3717(x^2-y^2)/a^2+6xy/a^2$ , where  $a$  is half the side length of the aperture. In the table,  $N$  is number of radial subapertures;  $M$  is the number of iterations;  $T_i$  is the computer time for the iterative solution;  $T_s$  is the serial computer time for matrix solution;  $T_p$  is the parallel computer time for the matrix solution. The iterative precision is 0.001,  $a=1$ .

$N$	$M$	$T_i$	$T_s$	$T_p$	$T_i/T_s$	$T_s/T_p$
2	4	0.0019	0.00034	0.00030	5.44	1.13
4	8	0.0058	0.00228	0.00035	2.55	6.53
6	15	0.0175	0.01058	0.00041	1.65	25.55
8	22	0.0398	0.03412	0.00060	1.17	57.04
10	28	0.0741	0.08074	0.00102	0.92	79.23
12	34	0.1251	0.17150	0.00212	0.73	80.80
14	40	0.1951	0.31036	0.00308	0.63	100.90
16	45	0.2811	0.54034	0.00469	0.52	115.27
18	51	0.4000	0.84696	0.00769	0.47	110.13
20	56	0.5353	1.28544	0.01228	0.42	104.65
30	81	1.6980				
50	125	7.1758				
100	215	49.4981				

## 7. Conclusions

The three reconstruction models proposed in this paper show no great difference in error propagation properties, among which, model III proves to have the best performance for its excellent uniformity of data sampling as well as for its algorithm that takes more factors into account.

The circular aperture is more advantageous than the square aperture in improving reconstruction precision probably because the former is better than the latter as to symmetry of subaperture arrangement.

Different solutions of the matrix equations produce a rather strong effect on the noise coefficient. The minimum mathematical power minimum norm solution turns out to have the highest precision; next comes the standard minimum mathematical power solution with zero phase point selected at the aperture center, while the standard minimum mathematical power solution with zero phase point selected on subaperture distribution angle is the poorest.

The parallel computational method can greatly increase the computational speed when used for the matrix solution in the case of a small number of subapertures. Yet when the subaperture number is large, an ordinary computer can by no means meet the storage load (internal storage) required under the matrix solution and in that case, the matrix iteration method must be used. To satisfy both computational precision and computational load, the zero-phase point might as well be selected at the aperture center for each iteration during iterative computations.

#### Acknowledgements

Thanks are due to my teachers Li Youping, Jiang Wenhan and Sun Jingwen for their instruction and assistance during my graduate thesis, from which some concepts in this paper are derived.

This paper was received for publication on May 15, 1989.

The revised paper was received on September 5, 1989.

#### References

- [1] W. H. Southwell, *JOSA*, 66, 998 (1980).
- [2] R. H. Hudgin, *JOSA*, 67, 375 (1977).
- [3] David L. Fried, *JOSA*, 67, 370 (1977).
- [4] 王开云, 大气湍流相位畸变校正的数值模拟, 中国工程物理研究院, (1989).

# Preliminary Experiments of Laser Beam Transmission with Adaptive Optics Compensating Atmospheric Turbulence

Jiang Wenhan, Yan Peiying, Dai Zichang and Li Bingcheng

(Institute of Optics & Electronics, Chinese Academy of Sciences)

**Abstract:** In this paper, the initial experimental results of laser beam transmission with the adaptive optics technique for compensating atmospheric turbulence is reported. With adaptive optics correction, the peak intensity at target plane is about 3.5 times of the peak intensity without correction.

**Key Words:** laser beam transmission, adaptive optics, atmospheric turbulence

When a laser beam propagates through the atmosphere, it tends to produce wavefront errors due to atmospheric turbulence. As a result, its divergence angle becomes much larger than the diffraction limit and its average irradiance becomes much lower than the value within the diffraction limit. Generally, when a coherent laser beam with wavelength  $\lambda$ , emitted from a transmission telescope with a diameter  $D$ , passes through the atmosphere with coherent length  $\gamma_0$  and arrives at a target with a distance  $L$ , its flare area is  $A$ , which, within the diffraction limit, is

$$A_{\text{ideal}} = (\lambda L/D)^2 \quad (1)$$

and can increase to

$$A = (\lambda L/D)^2 [1 + (D/r_0)^2] \quad (2)$$

where the unit of  $A_{\text{ideal}}$  and  $A$  is  $\text{m}^2$ , while other parametric units are all  $\text{m}$ . Correspondingly, the irradiance at the target will decrease to  $1/[1+(D/r_0)^2]$  times the value within the diffraction

limit. In this case, an adaptive optics system, by performing real-time correction of wavefront errors created by atmospheric turbulence, can make the flare at the target approach the diffraction limit.

Our recent preliminary experiment on laser transmission with an adaptive optics system [1] for atmospheric turbulence compensation demonstrated that the trial application of adaptive optics to a laser transmission system was successful.

Our experimental system is shown in Fig. 1. The system was mounted on top of a building, while a beacon light-source and a receiving target surface were installed on top of another building. The beacon light-source was a continuous 2.5mW He-Ne laser device. The horizontal distance between the beacon light-source and the experimental system was 340m, the horizontal height was approximately 15m, and atmospheric coherent length between them  $\gamma_0$  varied from 5 to 10cm. In the adaptive-optics system, a transverse shear interferometer was used as the wavefront detector to detect wavefront errors coming from the beacon light-source, which, after electrical processing, were deformed with a 21-unit deformable reflector (wavefront corrector) to compensate for the beacon beam wavefront errors (the system band was approximately 300Hz wide, i.e. enough to perform real-time compensation for atmospheric turbulence within 300Hz). When the transmitted laser beam passed through the deformable reflector and deflected from the optical path, it produced a wavefront conjugated with the erroneous wavefront caused by atmospheric turbulence. The erroneous wavefront, on passing through the atmosphere and reaching the target surface, was restored to the ideal wavefront and achieved compensation for the atmospheric turbulence (the target surface was placed at approximately 2m behind the beacon light-source,

where two beams were approximately 1cm apart, located, within

equal halo angle). Light spots on target surface were photographed with a CCD camera; energy distribution on target surface was analyzed and displayed with a computer and a TV image data collection system.

The experimental results are shown in Figs. 2 and 3. Fig. 2 displays the uncorrected target surface energy distribution, while Fig. 3 shows the target surface energy distribution after correction. It can be seen that target surface flares appear blurred prior to correction, consisting of numerous light spots, while after correction, the diffraction limit Ali flares appear distinct on the target surface. In terms of the three-dimensional energy distribution on the target surface, the corrected peak energy (light intensity) increases to approximately 3.5 times the value prior to correction, i.e. the energy (light intensity) distribution is close to the diffraction limit.

This research project is planned to continue.

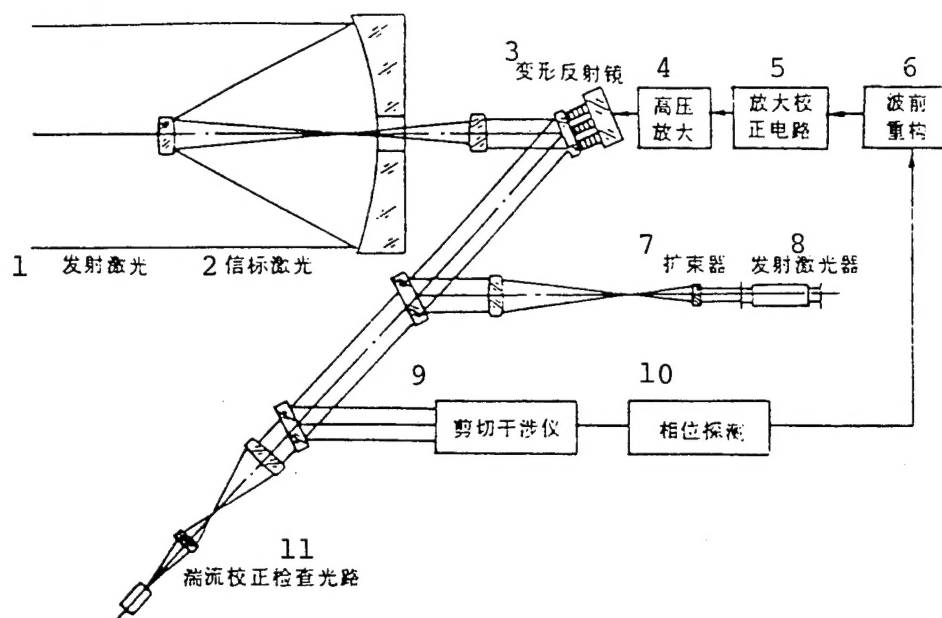
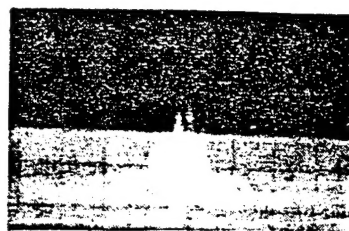


Fig. 1. Experimental system

Key: 1. Transmitted laser beam;  
 2. Beacon laser beam; 3. Deformable  
 reflector; 4. High voltage  
 amplification; 5. Amplified correction  
 circuit; 6. Wavefront reconstruction;  
 7. Beam expander; 8. Transmitting  
 laser device; 9. Shear interferometer;  
 10. Phase detection; 11. Optical path  
 for checking turbulence correction



(a) 像点



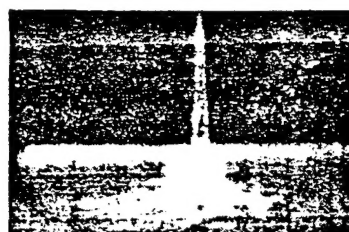
(b) 三维分布

Fig. 2 Energy Distribution on target surface before correction

(a) Image points; (b) Three-dimensional distribution



(a) 像点



(b) 三维分布

Fig. 3. Energy distribution on target surface after correction

(a) Image points; (b) Three-dimensional distribution

This paper was received for publication on October 5, 1989.  
The revised paper was received on November 29, 1989.